

## Regular Article

# Influence of 300 °C thermal conversion of Fe-Ce hydrous oxides prepared by hydrothermal precipitation on the adsorptive performance of five anions: Insights from EXAFS/XANES, XRD and FTIR (companion paper)



Natalia Chubar<sup>a,b,\*</sup>, Vasyi Gerda<sup>a,c</sup>, Dipanjan Banerjee<sup>d</sup>

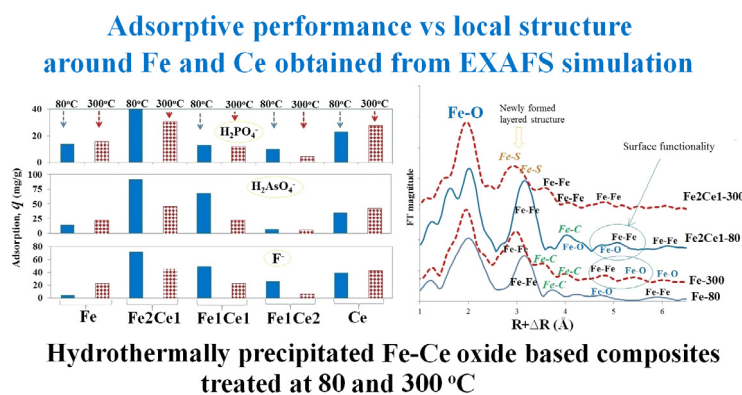
<sup>a</sup> Department of Earth Sciences, Faculty of Geosciences, Utrecht University, P.O. Box 80021, 3508 TA Utrecht, The Netherlands

<sup>b</sup> School of Engineering and Built Environment, Glasgow Caledonian University, Cowcaddens Road 70, Glasgow G40BA, United Kingdom

<sup>c</sup> Faculty of Chemistry, Kyiv National Taras Shevchenko University, 12 L. Tolstogo Str., 01033 Kyiv, Ukraine

<sup>d</sup> Dutch-Belgian Beamline (DUBBLE), ESRF – The European Synchrotron CS 40220, 38043 Grenoble Cedex 9, France

## GRAPHICAL ABSTRACT



## ARTICLE INFO

## Article history:

Received 31 October 2016

Revised 1 December 2016

Accepted 4 December 2016

Available online 7 December 2016

## Keywords:

Fe and Ce hydrous oxides

Urea precipitation

Thermal conversion

Adsorption

EXAFS

Toxic anions

## ABSTRACT

In this work, we report atomic-scale reconstruction processes in Fe-Ce oxide-based composites (hydrothermally precipitated at Fe-to-Ce dosage ratios of 1:0, 2:1, 1:1, 1:2, and 0:1), upon treatment at 300 °C. The structural changes are correlated with the adsorptive removal of arsenate, phosphate, fluoride, bromide, and bromate. The presence of the carbonate-based Ce-component and surface sulfate in precursor samples creates favorable conditions for phase transformation, resulting in the formation of novel (unknown) layered compounds of Fe and Ce. These compounds are of the layered double hydroxide type, with sulfate in the interlayer space. In spite of general awareness of the importance of surface area in adsorptive removal, the increase in surface area upon thermal treatment did not increase adsorption of the studied anions. However, EXAFS simulations and the adsorption tests provided evidence of regularities between local structures of Fe in composites obtained at 80 and 300 °C and adsorption performance of most studied anions. The best adsorption of tetrahedral anions was demonstrated by samples whose simulated outer Fe shells resulted from oscillations from both O and Fe atoms. In contrast, the loss of extended x-ray absorption fine structure was correlated with the decrease of adsorptive removal. Both Fe K-edge and Ce L<sub>3</sub>-edge EXAFS suggested the formation of solid solutions. For the first time, the utilization of extended x-ray absorption fine structure is suggested as a methodological approach (first

\* Corresponding author at: School of Engineering and Built Environment, Glasgow Caledonian University, Cowcaddens Road 70, Glasgow G40BA, United Kingdom.

E-mail address: [Natalia.Chubar@gnu.ac.uk](mailto:Natalia.Chubar@gnu.ac.uk) (N. Chubar).

expressed in the companion paper) to estimate the surface reactivity of inorganic materials intended for use as anion exchange adsorbents.

© 2016 Elsevier Inc. All rights reserved.

## 1. Introduction

It is well-known that new technologies in the 21st century are (often) based on using new materials. Metal oxides can form a wide variety of structural geometries and electronic structures that exhibit unique properties as adsorbents, catalysts, sensors, piezoelectric devices, fuel cells, coatings for the passivation of surfaces against corrosion, microelectronic circuits, and in medicine for disinfection [1–9]. These include ceria ( $\text{CeO}_2$ ) and iron oxides, both of which are important inorganic materials with great potential for a wide range of applications, partially due to their redox properties. One of the unique qualities of ceria is its reducibility from  $\text{CeO}_2$  to  $\text{CeO}_{2-x}$  under redox conditions, which makes it an excellent catalyst and catalytic support [10]. Success in some of these applications (such as adsorption and catalysis) depends, foremost, on the structural and electronic properties of the materials, while other properties (such as optical properties) are directly dependent on particle size. Emergent properties have been discovered at the interface with complex oxides, which are composed of several phases of different metal oxides. For example, the authors showed that a homogeneous  $\text{CeO}_2\text{-ZrO}_2$  solid solution exhibited the highest oxygen storage/release capacity among several types of  $\text{CeO}_2\text{-ZrO}_2$ , which was a function of their atomic structure [11,12]. Moreover, complex oxides based on multiple metal oxides have proved to be more efficient in such applications, compared to individual oxides of the same metals. For example,  $\text{Fe}_x\text{Ce}_{(1-x)}\text{O}_2$  mixed oxides were shown to exhibit synergistic catalytic activity for  $\text{N}_2\text{O}$  decomposition, by [13].

There are six main groups of adsorptive materials, which were developed in the following chronological order: carbons, zeolites, ion exchange resins, inorganic ion exchangers, composite/hybrid materials, and low-cost adsorbents (agricultural waste products, biomass, and industrial wastes). Two commercial inorganic ion exchangers entering the water market met the new WHO water standards for arsenic in 2004. Both of them are based on individual hydrous oxides,  $\text{Al}_2\text{O}_3$  and  $\text{Fe}_2\text{O}_3$ . However, Granular Ferric Hydroxide (GFH) demonstrates a much stronger capacity for arsenic removal, compared to activated alumina (AA). In contrast to AA, GFH has moderate crystallinity and includes several species of iron hydrous oxide. Since 2004, water and food industries have been subjected to many new purification tasks, which require continuous upgrade of material properties. Increasingly advanced materials can be developed from an improved understanding of the material chemistry in a particular synthesis and in the final product. It is also important to understand the reconstruction processes that result from major activation approaches, such as thermal and hydrothermal treatments of solid materials. Since the structural and electronic properties of materials define their adsorptive and catalytic activities, studies of the structure of materials should be conducted at the atomic scale. Thus, research tools for material characterisation should ideally examine both amorphous and crystalline phases.

Any potential application of a metal oxide starts from its preparation, including the choice of the synthetic approach/method and synthetic conditions. The method of preparation predetermines most (>70%) of the structural and electronic properties of the material. The chemical structure of co-precipitated Fe-Ce mixed oxides as a function of metal ratio and treatment temperature, reported

by Perez-Alonso and co-authors [14], differs considerably from that of Fe-Ce mixed oxides prepared by hydrothermal precipitation in this work. Hydrothermal precipitation is considered to be a major and powerful route for the preparation of metal oxides, and has gained increasing popularity in nanotechnology [15]. It allows broad variations in the structure/properties of materials by varying the synthetic conditions. Several individual Fe and Ce oxides have been prepared by this approach [16–19]. However, data on material structure as a function of Fe/Ce dosage ratio and preparation conditions are rare.

In the companion paper [20], we reported the materials chemistry, at synthesis and in the final solids of five inorganic composites, with various Fe-to-Ce ratios at dosage (0:1; 1:1; 1:2; 2:1, and 1:0), and dried at 80 °C. We explained the reasons for variations in the selectivity of anion removal of five composites, based on their structure and surface chemistry. In this work, we report phase and atomic-scale transformations in the same materials upon thermal treatments at 300 °C, and link the preferential adsorptive properties of these materials to the same five toxic anions studied in the companion paper. This strategy/way suggests a novel methodological approach to estimate the anion-removal properties of inorganic ion exchangers, by focusing on outer shells of extended local structure around the major atoms composing the adsorbent. We expect this methodological approach to be useful for estimating the catalytic performances of the relevant reactions, and future work might include testing for applicability in catalysis.

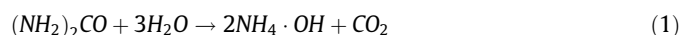
This work is the first atomic-scale study of reconstruction processes in Fe-Ce oxide-based composites upon thermal treatment at 300 °C. It is also the first study of phase transformations of hydrothermally precipitated Fe-Ce bimetal oxides as a function of Fe-to-Ce dosage ratios, upon thermal treatment at 300 °C.

## 2. Materials and methods

### 2.1. Preparation of materials

The Fe-Ce hydrous oxide-based composites were prepared under urea ( $\text{CO}(\text{NH}_2)_2$ )-based hydrothermal conditions by co-precipitation from aqueous iron(II) and cerium(III) sulfate solutions. The chemicals ( $\text{FeSO}_4 \cdot 7\text{H}_2\text{O}$ ,  $\text{Ce}_2(\text{SO}_4)_3$  and  $\text{CO}(\text{NH}_2)_2$ ) used in this work were purchased from Sigma-Aldrich. The synthesis procedure was based on few stages. First, calculated quantities of the chemicals were dissolved in 700 ml of distilled water and stirred for 10 min. The solution was moved into a 1000 ml autoclave with a Teflon liner and maintained without agitation at 120 °C for 24 h, then cooled to room temperature. The precipitate was filtered, washed several times with generous amount of distilled water till negative reaction of sulfate, and then with alcohol (ethanol), and dried first at ambient temperature ( $20 \pm 2$  °C) and then thermally treated at 300 °C in thermolyne benchtop muffle furnace (Sigma-Aldrich). The samples shown for comparison (and reported in the companion paper) were also dried at ambient temperature and then at 80 °C.

The materials chemistry of the synthesis is underpinned by the release of  $\text{OH}^-$  and  $\text{CO}_2$  into the aqueous medium, via the decomposition of urea, according to (1):



Five dosage ratios of Fe(II)/Ce(III) were applied for synthesis: 1Fe:0Ce, 2Fe:1Ce, 1Fe:1Ce, 1Fe:2Ce, and 0Fe:1Ce, at the same concentration of urea and total volume of reagents. (The products resulting from each of these syntheses are denoted here as Fe, Fe2-Ce1, Fe1-Ce1, Fe1-Ce2, and Ce). The synthetic conditions are shown in Table 1.

The temperature of 300 °C was chosen for the thermal treatment to maximize formation of the pure phases of metal hydrous oxides (most relevant chemical nature to sorb anions) by minimizing the content of carbonate phases, and at the same time to preserve as much as possible the surface functionality shown in (OH<sup>−</sup>) groups. High temperature can reduce the concentration of surface functional groups (OH<sup>−</sup>) which might result in decrease of adsorptive removal of the most anions. Therefore, having in mind the application of these materials in adsorption we decided to test the temperature of 300 °C and to see how it is reflected on the material properties and adsorption.

## 2.2. Structural characterization techniques

The chemical composition of the bulk samples was determined by dissolving the samples in acid, followed by measurements of Fe and Ce concentrations by a Spectro CIROS<sup>CCD</sup> ICP-OES with radial plasma (Spectro A.I., Germany). Carbon analysis was conducted by a Carlo-Erba, Model 1106 CHN elemental analyzer. XRD measurements were conducted using a Bruker-AXS D8 Advance powder X-ray diffractometer equipped with an automatic divergence slit, a Vantec-1 detector, and a CoK $\alpha$ 1,2 ( $\lambda$  = 1.79026 Å) source. FTIR spectra were collected within the range of 400–4000 cm<sup>−1</sup> on a Nicolet 6700 Fourier transform infrared (FT-IR) spectrometer, using the conventional KBr pellet method in transmission mode. BET surface area and porosity were analyzed by the N<sub>2</sub>-adsorption method at liquid nitrogen temperature (77 K) in a Micromeritics Tristar 3000 (USA). Prior to the nitrogen adsorption measurements, each sample (approximately 150 mg in weight) was degassed at 120 °C for 14 h in vacuum. The BET surface area was determined by using the N<sub>2</sub> adsorption data under a relative pressure ( $P/P_0$ ) range of 0.05–0.25. The total pore volume for single-point adsorption was obtained from the adsorption isotherm at  $P/P_0 \approx 0.995$ . TriStar 3000 V6.00 software was used for all calculations, based on isotherm data. This software can apply t-plot micropore analysis (based on de Boer model) and the BJH (based on Barret-Joyner-Halenda) adsorption/desorption model. XPS spectra were recorded with an Axis Ultra DLD electron spectrometer (Kratos Analytical, UK), using a monochromated Al K $\alpha$  source operated at 150 W.

Fe K-edge (7112 eV) and Ce L<sub>3</sub>-edge (5723 eV) EXAFS/XANES spectra were recorded at the Dutch-Belgian (DUBBLE) beamline (BM26A) of European Synchrotron Radiation Facilities (ESRF), Grenoble, France. The beamline was equipped with a Si(111) double-crystal monochromator. All measurements were performed in the transmission detection mode at room temperature. A contemporary experimental setup of the DUBBLE beamline has been described in [21]. The Athena, Artemis, and Atoms software

packages were used to process and model the EXAFS data [22]. The linear combination fitting (LCF) option of Athena was applied to estimate compositions of the composites and the ratios of various compounds. LCF was based on XANES (EXAFS) of the experimental reference materials, collected at the same beam, DUBBLE: Ce<sub>2</sub>(CO<sub>3</sub>)<sub>3</sub>, CeO<sub>2</sub>, Ce(OH)<sub>4</sub>, FeOOH, Fe<sub>2</sub>O<sub>3</sub>, FeO, FeCO<sub>3</sub>, Fe(II)/Fe(III) oxide. Feff.inp files were generated using the crystallographic data of several relevant compounds:  $\alpha$ -Fe<sub>2</sub>O<sub>3</sub> (hematite),  $\beta$ -iron oxide, siderite (FeCO<sub>3</sub>) [23], goethite (layered Fe(II)/Fe(III) oxide) [24] and butlerite (Fe(II)/Fe(III) green rust) [25], CeO<sub>2</sub> [26], Ce<sub>2</sub>(CO<sub>3</sub>)<sub>3</sub> [27], Ce(OH)CO<sub>3</sub> [28], and Ce(OH)SO<sub>4</sub> [29]. The paths were plotted together with the experimental spectra, carefully considered and selected for the final fits. Scattering of heavy and light atoms was distinguished by changes in K-weighting and empirically (using the Artemis software, which distinguishes oscillations from heavy (Fe-Fe) and light (Fe-O) chemical elements). The FT peaks were fit stepwise, starting from the first shell. More paths (using crystallography data of various compounds) were added stepwise, to include and fit the next shell.

## 2.3. Batch adsorption characterization and analytical chemistry measurements

Batch adsorption tests were performed at ambient temperature and pH = 6.7 ± 0.2 (adjusted during experiments, using 0.1 N HNO<sub>3</sub> and NaOH). The initial concentrations of several anions (H<sub>2</sub>PO<sub>4</sub><sup>−</sup>, H<sub>2</sub>AsO<sub>4</sub><sup>−</sup>, F<sup>−</sup>, Br<sup>−</sup> and BrO<sub>3</sub><sup>−</sup>) were 200 ± 15 mg/L, measured as, for example, mg[As]/L. Batch adsorption experiments were conducted in 50 ml polyethylene tubes, using an adsorbent dose (solid/liquid ratio) of 2 g/L and 0.1 N NaNO<sub>3</sub> as background electrolyte until equilibrium. Exactly 40 (±2) mg of the adsorbent was added to 20 ml of the adsorbate. Samples of the adsorbate were filtered, and the concentrations of P, As, Fe, and Ce were measured by ICP-OES. The concentrations of F<sup>−</sup>, Br<sup>−</sup> and BrO<sub>3</sub><sup>−</sup> were measured by ion chromatography. Adsorption was calculated by the standard empirical formula:

$$q = \frac{(C_0 - C_{eq})V}{m}, \quad (2)$$

where  $q$  (mg/g<sub>dw</sub>) is the amount of anion sorbed per gram of adsorbent (dry weight),  $C_0$  (mg/L) is the initial concentration of the anion (as P, As, Br, or F),  $C_{eq}$  (mg/L) is the final (or equilibrium) concentration of the anion in solution,  $V$  (mL) is the volume of the solution, and  $m$  (mg<sub>dw</sub>) is the dry weight of the adsorbent.

## 3. Results

### 3.1. Chemical compositions and porous structure of new composites

Thermal treatment of the inorganic composites at 300 °C caused a number of changes in the chemical composition and surface chemistry of these materials, compared with samples prepared from the same synthetic batch at 80 °C and replotted in the companion paper, see Table 1. The Fe/Ce ratio was almost unchanged

**Table 1**

Synthetic conditions and composition of Fe-Ce oxide-based composites (synthesized at 300 °C), based on chemical & CHN analysis, and surface analysis by XPS.

Sample	Ratio in solution	Chemical composition in solid, %					XPS surface analysis, at.%		
	Fe <sup>2+</sup> /Ce <sup>3+</sup> /Urea/H <sub>2</sub> O, Moles	Fe	Ce	C	H	Fe <sup>2+</sup> /Ce <sup>3+</sup> ratio	Fe <sup>2+</sup> /Ce <sup>3+</sup> ratio	C, (CO <sub>3</sub> <sup>2−</sup> )	S, (SO <sub>4</sub> <sup>2−</sup> )
Fe	0.06/0.0/0.16/40.0	61.02	–	0.35	0.62	–	–	1.8	2.5
Fe2-Ce1	0.04/0.02/0.16/40.0	25.31	37.67	0.10	0.38	1.69/1.0	5.8	0.9	3.7
Fe1-Ce1	0.03/0.03/0.16/40.0	15.91	57.47	0.13	0.50	1.0/1.44	5.5	2.3	trace
Fe1-Ce2	0.02/0.04/0.16/40.0	12.86	66.8	0.19	0.33	1.0/2.07	1.5	5.8	trace
Ce	0.0/0.06/0.16/40.0	–	79.96	0.56	0.44	–	–	8.6	2.2

n = 2;3, m = 3;4.

when the Fe-Ce dosage was equal (Fe1-Ce1). On the other hand, samples with one dominant metal, i.e., Fe2-Ce1 and Fe1-Ce2, were characterized by increased Fe contents. The concentration of bulk carbon (CHN analysis) was reduced from ~2.5–4.6% to <0.5%; more specifically, to 0.1–0.2% in two-metal samples and 0.35/0.56% in the one-metal samples Fe and Ce, respectively. Surface carbon (as carbonate) in the purely Fe-based sample was almost unchanged. However, in the remaining samples treated at 300 °C, it was reduced 2–3 times in comparison with the samples treated at 80 °C.

Fig. S1 (Supplementary supporting information, SI) shows  $N_2$  adsorption/desorption isotherms and pore diameter data which are partly presented in Table 2. Table 2 shows that thermal treatment of the composite at 300 °C resulted in the highest crystallinity compared to the materials dried at 80 °C. The surface area of Fe was not changed. However, there was an increase in pore volume (from 0.17 to 0.23 cm<sup>3</sup>/g) and a decrease in BJH des. av. pore diameter (from 6.8 to 3.7 nm). On the other hand, thermal treatment of the other samples resulted in a considerable increase in  $S_{BET}$ . The increase in surface area was proportional to the percentage of the Ce-phase in the samples treated at 80 °C, based on various species of Ce carbonate compounds. Interestingly, in spite of the unchanged or considerably enlarged  $S_{BET}$  surface area and pore volume, the average pore diameter for BJH desorption

decreased, except for one sample that was based purely on Ce-compounds.

### 3.2. Crystalline phases of the Fe-Ce oxide-based composites from XRD patterns

The XRD patterns are shown in Fig. 1; full XRD data (Tables S1–S5) are shown in Supporting Information (SI). Table 3 lists the crystalline phases in the composites, inferred from XRD patterns on the basis of the XRD database and literature. The XRD patterns showed several major changes in the compositions of the crystalline phases, resulting from the treatment at 300 °C. Firstly, one new Fe-oxide-based and one new Ce-oxide-based phases were formed in all samples, in particular, hematite, and ceria (see Table 3). The most crystalline sample from treatment at 80 °C (based on solo-Fe compounds) showed a reduced degree of crystallinity (an estimate is based on the intensity). In contrast, the degree of crystallinity of the Ce-sample was not changed but increased dramatically in the three bimetal materials. Importantly, the high crystallinity of Fe-Ce samples originated in the unknown phase(s). We refer to this phase as a new phase(s) of layered Fe/Fe and/or Fe-Ce hydrous oxides, containing sulfate and carbonate in the interlayer.

**Table 2**  
Structural parameters of Fe-Ce oxide/carbonate-based materials dried at 80 °C and thermally treated at 300 °C.

Sample	Surface area, m <sup>2</sup> /g			V, cm <sup>3</sup> /g	BJH des. av. pore diameter (4V/A), nm
	$S_{BET}$ , mg/g	T-Plot micropore area	T-Plot external area		
Fe-80	103	31	72	0.17	6.8
Fe-300	107	36	71	0.23	3.7
Fe2-Ce1-80	49	–	49	0.21	14.2
Fe2-Ce1-300	73	28	45	0.14	8.2
Fe1-Ce1-80	37	4	33	0.14	12.7
Fe1-Ce1-300	114	41	73	0.21	8.0
Fe1-Ce2-80	29	2	27	0.12	14.6
Fe1-Ce2-300	101	28	73	0.28	12.2
Ce-80	11	3	8	0.03	3.9
Ce-300	81	60	21	0.07	3.7

Note: samples dried at 80 °C, shown in the companion paper [20], are denoted as “x-80”. The composites that were thermally treated at 300 °C (the subject of the present work) are denoted as “x-300”.

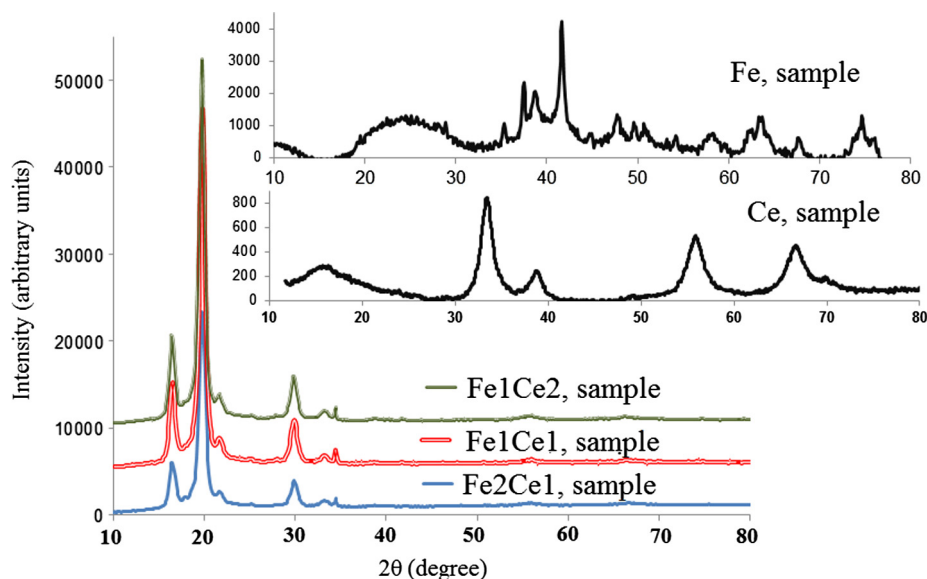


**Fig. 1.** XRD patterns of Fe-Ce oxide-based composites, thermally treated at 300 °C.

**Table 3**

Crystalline phases from XRD patterns of Fe-Ce oxide-based composites treated at 80 [20] and 300 °C (see full XRD data in SI, Tables S1–S5).

	Samples, thermally treated at 80 °C				
	Fe	Fe2-Ce1	Fe1-Ce1	Fe1-Ce2	Ce
<i>Fe-phase</i>					
Maghemite, $\gamma$ -Fe <sub>2</sub> O <sub>3</sub>	✓	✓	✓	✓	n/a
Magnetite, Fe <sub>3</sub> O <sub>4</sub>	✓	✓	✓	–	n/a
Siderite, FeCO <sub>3</sub>	✓	Amorphous, EXAFS	–	–	n/a
<i>Ce-phase</i>					
Ce <sub>2</sub> O(CO <sub>3</sub> ) <sub>2</sub> ·H <sub>2</sub> O	n/a	✓	✓	✓	✓
Ce(OH)CO <sub>3</sub>	n/a	–	–	✓	✓
Samples, thermally treated at 300 °C					
<i>Fe-phase</i>					
Hematite, $\alpha$ -Fe <sub>2</sub> O <sub>3</sub>	✓	✓	✓	✓	n/a
Maghemite, $\gamma$ -Fe <sub>2</sub> O <sub>3</sub>	✓	✓	✓	✓	n/a
Ferrihydrite (Fe <sub>5</sub> O <sub>7</sub> (OH)·4H <sub>2</sub> O)	✓	–	–	–	n/a
Siderite, FeCO <sub>3</sub>	✓	–	–	–	n/a
<i>Ce-phase</i>					
CeO <sub>2</sub>	n/a	✓	✓	✓	✓

EXAFS and FTIR studies presented further evidence confirming these results. Overall, the Ce-component, which was completely based on various species of Ce carbonate in the samples at 80 °C, was fully transformed into CeO<sub>2</sub> upon thermal treatment at 300 °C. The Ce-component was represented by one crystalline phase only. In contrast, there were several crystalline phases of the Fe component in two-metal composites and in sample Fe. Interestingly, siderite, which was one of the crystalline phases in the Fe sample treated at 80 °C, was not decomposed completely by thermal treatment at 300 °C (Table 3). The total content of FeCO<sub>3</sub> was reduced from 20.6 to 9.5%, as shown by XANES LCF. Most of the iron carbonate species were most probably crystalline (siderite), which was why they were not decomposed to the same extent as the cerium carbonate species.

### 3.3. Fe oxidation state and composition of Fe-component from XANES

XANES of Fe K-edge EXAFS covering both crystalline and amorphous phases of the Fe-component (Fig. 2) demonstrated that the

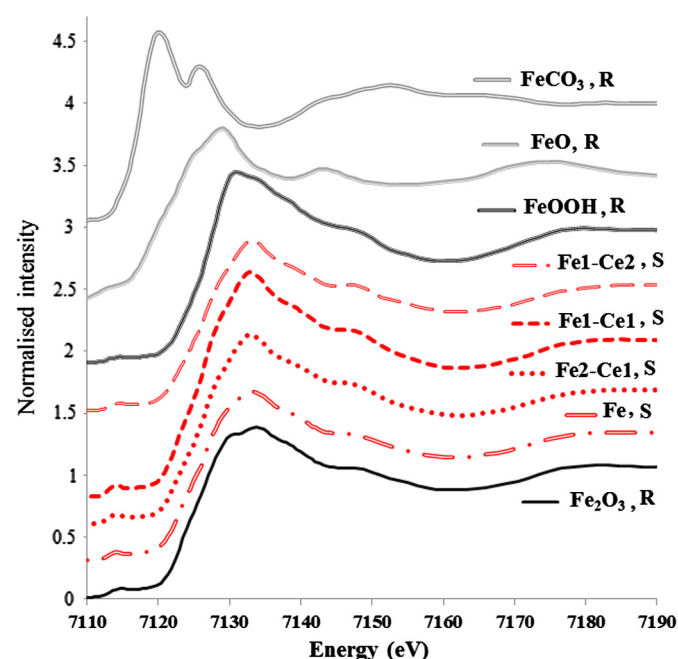


**Fig. 2.** XANES of Fe-components of samples (S) treated at 300 °C and the references (R).

**Table 4**

Estimate of phase composition from the LCF of Fe-components of the samples treated at 80 and 300 °C, respectively, % of reference compound.

	Fe, S		Fe2-Ce1, S		Fe1-Ce1, S		Fe1-Ce2, S	
	80 °C	300 °C	80 °C	300 °C	80 °C	300 °C	80 °C	300 °C
FeCO <sub>3</sub> , R	20.6	9.5	4.7	–	–	–	–	–
FeOOH, R	40.6	–	95.3	75.0	57.9	9.9	55.8	17.6
Fe <sub>2</sub> O <sub>3</sub> , R	34.9	–	–	25.0	14.2	87.9	36.2	5.6
Fe(III)oxide, R	–	87.7	–	–	–	2.2	–	76.8
FeO, R	–	–	–	–	–	–	8.0	–
Fe(II)Fe(III) Oxide, R	3.9	–	–	–	27.9	–	–	–
Unknown	–	2.8	–	–	–	–	–	–

\*\*S – sample, R – reference.

Fe-component was mainly composed of Fe(III) hydrous oxides. The detection limit of XANES did not allow visual detection of FeCO<sub>3</sub> in any of the four samples.

Focus was placed on the pre-edge region and the first inflection points of XANES spectra of the samples and references, to obtain an insight into the oxidation state of Fe (Figs. S2 and S3) and particularly, to estimate whether Fe exists partially as Fe<sup>2+</sup>. The detection limit of XANES did not allow the detection of the small content of Fe(II) in the structure, based on the pre-edge analysis. However, the first inflection point data (Fig. S3B) suggested a minor presence of Fe<sup>2+</sup> in these three samples. LCF, based on six available references (Fig. S4 and Table 4), demonstrated that all Fe oxide-based compounds were based on various species of hydrous oxides of Fe, and the species of iron oxides were different in different samples. The presence of FeCO<sub>3</sub> (9.5%) was also confirmed in the 300 °C-Fe sample, while it was absent in bimetal samples.

### 3.4. Ce oxidation state and composition of Ce-component from XANES

XANES of the Ce component, shown in Fig. 3, evidenced that the main Ce-based compounds were Ce(IV) hydrous oxides. However, a small shoulder at approximately 5720 eV, which was most obvious in the Ce sample, indicated the possible presence of other phases, one of which might be Ce(III) carbonate (see the references in Fig. 3). Consideration of the pre-edge region and the first inflection point of the XANES derivatives (see Figs. S5 and S6) suggested that the percentage of Ce(III) in the Ce-component was lower than 20%. This was in agreement with the LCF results. LCF demonstrated that the main phases of the Ce-component were Ce(IV) hydrous oxides. The presence of small quantities of Ce<sub>2</sub>(CO<sub>3</sub>)<sub>3</sub> was also

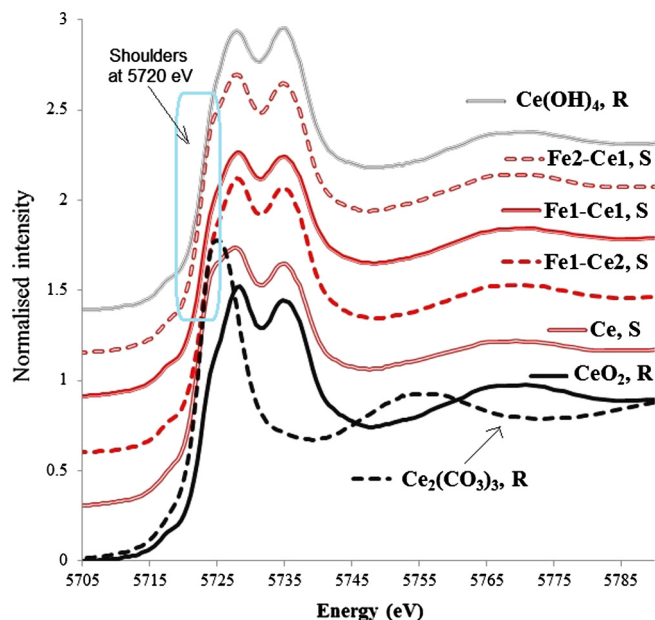


Fig. 3. XANES of Ce-components of the samples (S) treated at 300 °C and the references (R).

confirmed (Table 5 and Fig. S7). Notably, cerium carbonate was not detected in XRD patterns, demonstrating its amorphous nature.  $\text{Ce}_2(\text{CO}_3)_3$  in the 300 °C-samples was a minor phase, resulting from the decomposition of the other species of Ce carbonate, which were transformed mainly into  $\text{CeO}_2$ . The  $\text{Ce}_2(\text{CO}_3)_3$  content was greater in the pure Ce-based material (18.3%) than in the two-metal samples (2.1–6.6%).

### 3.5. Local structure around Fe atom, obtained from EXAFS simulations

Fe K-edge EXAFS spectra of composites and one experimental reference ( $\text{Fe}_2\text{O}_3$ ) are shown in Fig. S8. Fig. 4 shows the radial structure around the Fe atom, obtained from Fourier transforms of Fe K-edge EXAFS oscillations. Additionally, it shows the fits generated on the basis of feff.inp files, obtained from crystallographic data of the relevant compounds. Table 6 summarizes results of EXAFS fitting, based on the paths shown in Table S6. These data are accompanied by a visual representation of distances between the Fe and the backscattering atoms, as shown in Fig. S9A.

Refinement of the local structure around Fe and the EXAFS fitting strategy (choice of paths from crystallographic data to achieve the best fit) reflected the atomic-scale changes resulting from thermal treatment. Interestingly, the first shells (Fe-O) of samples Fe and Fe2-Ce1 were fit by two Fe-O paths. In contrast, the first shells of the Fe absorber in Fe1-Ce1 and Fe1-Ce2 (which were dominated by the Ce component) were best fitted with 6 O atoms each at 2.00 and 1.95 Å, respectively, using only one Fe-O path. Fe-O distances in the Fe sample resembled those in hematite (whose crystallographic Fe-O distances are 1.95 and 2.12 Å [23]), while the first

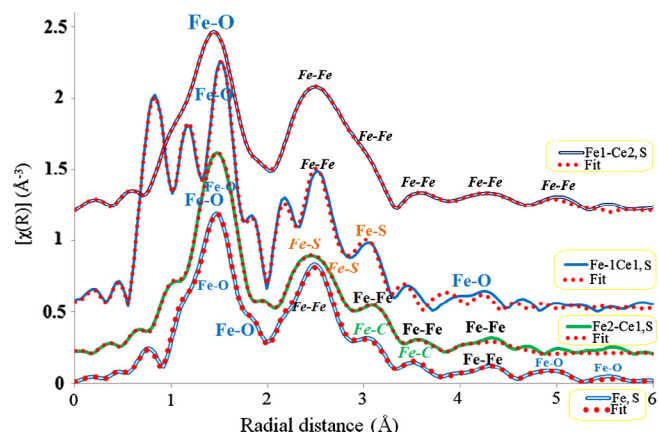


Fig. 4. Radial structure around Fe, obtained from Fourier transforms of Fe K-edge EXAFS oscillations of the experimental samples and their fits.

shell of Fe2-Ce1 treated at 300 °C was best simulated with two Fe-O paths of layered guildite (whose crystallographic Fe-O distances were 1.97 and 2.00 Å) [24]. The R-factor, which indicates the degree of disorder, was higher for all samples with a higher percentage of Ce compounds. It was calculated to be 0.0014, 0.0028, and 0.0036 for Fe2-Ce1, Fe1-Ce1, and Fe1-Ce2, respectively. The R-factor was correlated with the pore volume: the higher the R-factor, the larger was the pore volume.

The second shells of Fe in all samples (at 3–4 Å) were the result of backscattering from several atoms, one of which was Fe. The combination of paths used to achieve good fits reflects the basic trends of material structure, and this information correlates with the data collected by other methods. In the Fe sample, the Fe-Fe distance was measured as 3.02 Å, which is close to the Fe-Fe distance in hematite (2.97 Å). In this sample, the Fe-C distance was measured as 3.72 Å, which confirms the minor presence of  $\text{FeCO}_3$ . A minor (second) Fe-C path of complex geometry had to be applied to fit two peaks resulting from C backscattering to the Fe absorber (Fig. 4). The 2nd shell of Fe2-Ce1 was refined with 2.0 and 2.5 atoms of S at 3.0 and 3.16 Å, and with 6 Fe atoms at 3.48 Å. None of these parameters resemble those of guildite. However, they reflect the regularity of the local structure. It must be noted that the characteristic Fe-S distances of guildite are 3.23 and 3.30 Å, and its Fe-Fe distance is 3.56 Å.

The local structure around Fe in the second shell of Fe1-Ce1 reflected the presence of both hematite and guildite, as suggested by their measured characteristic Fe-Fe and Fe-S distances of 3.06 and 3.21 Å, respectively. However, in spite of the similarity of XRD patterns of the three bimetal samples, the Fe-S distance could not be measured in Fe1-Ce2. The most probable reason for this is the dominance of backscattering from heavier (Fe and Ce) atoms over oscillations from the lighter atoms (such as S), which makes the latter “invisible” in EXAFS. The local structure around Fe in Fe1-Ce2 was fully simulated by Fe-Fe paths, one of which was characteristic of hematite (3.01 Å) while the second was a mean of Fe-Fe distances in hematite and guildite.

Table 5

Estimate of phase composition from the LCF of Ce-components of the samples treated at 80 and 300 °C, respectively, % of a reference compound.

	Ce, S		Fe1-Ce2, S		Fe1-Ce1, S		Fe2-Ce1, S	
	80 °C	300 °C	80 °C	300 °C	80 °C	300 °C	80 °C	300 °C
$\text{Ce}_2(\text{CO}_3)_3$ , R	95.6	18.3	92.9	4.0	100	2.1	100	6.6
$\text{Ce}(\text{OH})_4$ , R	4.4	36.4	7.1	50.3	–	63.8	–	64.1
$\text{CeO}_2$ , R	–	45.3	–	45.7	–	34.1	–	29.3

\*\*S – sample, R – reference.

**Table 6**

Curve fitting results of Fe K-edge EXAFS of 300 °C-samples Fe, Fe2-Ce1, Fe1-Ce1, and Fe1-Ce2. See the crystallographic data used for the fits in Table S6. R—interatomic distance, CN—coordination number,  $\sigma^2$ —Debye–Waller mean square disorder factor,  $\Delta E_0$ —energy shift parameter, R-factor—goodness of fit.

Sample	Path and relevant crystallographic information	R (Å)	CN	$\sigma^2$ (Å <sup>2</sup> )	$\Delta E_0$ (eV)	R-factor
Fe	Fe-O (hematite)	1.94	3.0	0.0045	4.36	0.0168
	Fe-O (hematite)	2.07	3.0	0.0087	−8.42	
	Fe-Fe (hematite)	3.02	6.0	0.0138	3.86	
	Fe-C (siderite)	3.72	2.0	0.0013	0.53	
	Fe-Fe (siderite)	4.75	2.0	0.0164	9.99	
	Fe-O (butlerite)	5.47	2.0	0.0188	2.81	
	Fe-O (siderite)	5.77	48.0	0.0169	3.28	
Fe2-Ce1	Fe-O (guildite)	1.97	4.0	0.0039	6.74	0.0014
	Fe-O (guildite)	2.09	2.0	0.0052	−8.14	
	Fe-S (guildite)	3.00	2.5	0.0001	−6.97	
	Fe-S (guildite)	3.16	2.0	0.0063	−4.33	
	Fe-Fe (guildite)	3.48	6.0	0.0089	3.71	
	Fe-Fe (hematite)	4.00	2.0	0.0033	−1.19	
	Fe-Fe (hematite)	5.04	2.0	0.0364	−9.97	
Fe1-Ce1	Fe-O (hematite)	2.00	6.0	0.0106	2.17	0.0028
	Fe-Fe (hematite)	3.06	4.0	0.0196	9.99	
	Fe-S (guildite)	3.21	4.0	0.0101	−4.06	
	Fe-O (guildite)	4.83	12.0	0.0222	−9.52	
Fe1-Ce2	Fe-O (hematite)	1.95	6.0	0.0156	−6.77	0.0036
	Fe-Fe (hematite)	3.01	3.0	0.0119	1.64	
	Fe-Fe (hematite)	3.42	6.0	0.0089	−1.52	
	Fe-Fe (hematite)	4.15	2.0	0.0346	5.03	
	Fe-Fe (hematite)	5.05	6.0	0.0131	−7.25	
	Fe-Fe (hematite)	5.62	6.0	0.0464	4.48	

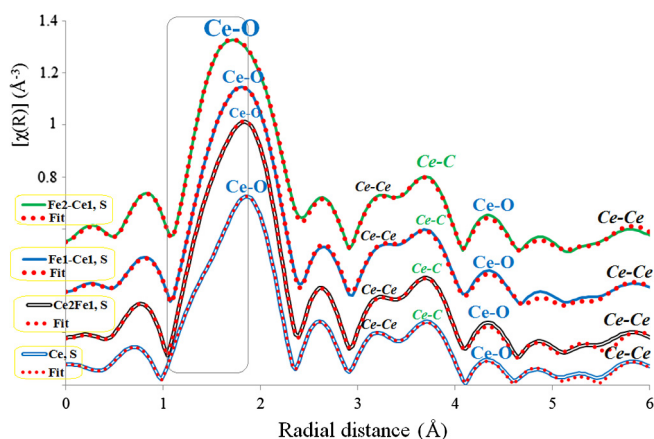


**Fig. 5.** Radial structure around Ce, obtained from Fourier transforms of EXAFS oscillations of the experimental samples and the experimental reference.

It is notable that the changes resulting from thermal treatment were also reflected in the local structure around Fe (at  $>3.5$  Å) (see the companion paper [20]). In particular, these changes included the formation or loss of the extended structure formed by backscattering from outer shells. Interestingly, the extended structure of the 300 °C-Fe sample was characterized by two new peaks at 5.47 and 5.77 Å, resulting from O oscillation backscattering, compared with the 80 °C-Fe composite. The outer shells of Fe in the two best 80 °C-adsorbents (Fe2Ce1 and Fe1-Ce1) were rich in O oscillation backscattering. However, the extended structure around Fe was lost upon thermal treatment. These observations suggest that the absence or lack of backscattering from O to Fe in the extended region might indicate partial loss of surface functionality, which might reduce the adsorptive removal of some anions.

Interestingly, the features of Fe K-edge EXAFS spectra in the  $k$ -space at 7–8 and 9 Å<sup>−1</sup> (Fig. S8) resembled those of green rust, studied in [30]. This confirms our assumption about the formation

of layered Fe/Ce-based hydrous oxides in the two-metal oxide structures.

### 3.6. Local structure around Ce atom, obtained from EXAFS simulations

The Ce L<sub>3</sub>-edge EXAFS spectra are shown in Fig. S10. Fig. 5 shows Fourier transforms of the experimental EXAFS functions at the Ce L<sub>3</sub>-edge. The results of EXAFS fitting are summarized in Table 7, along with Table S7 (which shows the paths applied to simulate the local structure around Ce) and Fig. S9B. Overall,

**Table 7**

Curve fitting results of Ce L<sub>3</sub>-edge EXAFS of Fe, Fe2-Ce1, Fe1-Ce1, and Fe1-Ce2 treated at 300 °C. See the crystallographic data used for the fits in Table S7. R—interatomic distance, CN—coordination number,  $\sigma^2$ —Debye–Waller mean square disorder factor,  $\Delta E_0$ —energy shift parameter, R-factor—goodness of fit.

Sample	Path and relevant crystallographic information	R (Å)	CN	$\sigma^2$ (Å <sup>2</sup> )	$\Delta E_0$ (eV)	R-factor
Ce	Ce-O (CeO <sub>2</sub> )	2.31	8.0	0.0120	5.27	0.0028
	Ce-Ce (CeO <sub>2</sub> )	3.66	12.0	0.0090	−9.99	
	Ce-C (Ce(OH)CO <sub>3</sub> )	3.91	2.0	0.0001	−0.94	
	Ce-O (CeO <sub>2</sub> )	4.55	12.0	0.0530	0.45	
	Ce-Ce (Ce(OH)SO <sub>4</sub> )	6.53	6.0	0.0017	5.09	
Fe1-Ce2	Ce-O (CeO <sub>2</sub> )	2.29	8.0	0.0106	4.21	0.0021
	Ce-Ce (CeO <sub>2</sub> )	3.70	12.0	0.0145	−5.93	
	Ce-C (Ce(OH)CO <sub>3</sub> )	3.96	2.0	0.0025	−4.26	
	Ce-O (CeO <sub>2</sub> )	4.29	12.0	0.0331	−5.70	
	Ce-Ce (Ce(OH)SO <sub>4</sub> )	6.60	2.0	0.0034	9.53	
Ce1-Fe1	Ce-O (CeO <sub>2</sub> )	2.29	8.0	0.0124	4.25	0.0011
	Ce-Ce (CeO <sub>2</sub> )	3.70	12.0	0.0333	−2.37	
	Ce-C (Ce(OH)CO <sub>3</sub> )	4.00	3.0	0.0030	5.44	
	Ce-O (CeO <sub>2</sub> )	4.95	12.0	0.0310	3.82	
	Ce-Ce (Ce(OH)SO <sub>4</sub> )	6.46	10.0	0.0188	1.75	
Fe2-Ce1	Ce-O (CeO <sub>2</sub> )	2.25	8.0	0.0165	−0.90	0.0048
	Ce-Ce (CeO <sub>2</sub> )	3.72	12.0	0.0259	−4.28	
	Ce-C (Ce(OH)CO <sub>3</sub> )	4.01	3.0	0.0053	2.61	
	Ce-O (CeO <sub>2</sub> )	4.50	12.0	0.0044	10.00	
	Ce-Ce (Ce(OH)SO <sub>4</sub> )	6.37	2.0	0.0182	9.99	

thermal treatment caused the decomposition of Ce-carbonate-based substances and transformed them mainly into  $\text{CeO}_2$ . However, a small amount of amorphous cerium carbonate was left in the structure. Easy transformation of  $\text{Ce}(\text{OH})\text{CO}_3$  into  $\text{CeO}_2$  was also reported by Qian and colleagues [31] and such transformations were expected and included in the experimental design.

Fig. 5 shows that the local structure around Ce was similar in all samples. However, the geometries of the first shell in the two-metal composites differed from the one-metal sample, Ce. The radial structure around Ce was simulated by applying the same fitting strategy to all samples. The first shell was modeled with 8 O atoms at 2.31, 2.29, and 2.25 Å in Ce, Fe1-Ce2/Fe1-Ce1, and Fe2-Ce1, respectively. These data demonstrate that the greater portion of the Fe-based compound in the composites shortened the Ce-O distances in the 1st shells, Fig. S9B. Fig. S9B graphically presents the distances from the absorber Ce to the backscattering atoms, O, C, and Ce/Fe in the 1st (1), 2nd (2), and outer (3) shells. At the same time, the 1st-shell geometries of the two-metal samples were broader than those based on Ce-compounds, which suggests the presence of Fe and the formation of solid solutions. The Fe-O distances in Fe oxides were shorter than the Ce-O distances in Ce-oxides.

The second shells, comprised of two peaks (at 3–4 Å), were fitted with two {Ce-Ce}+{Ce-C} paths. In contrast to the 1st shell, a greater amount of Fe-containing materials in the composites resulted in longer Ce-Ce and Ce-C distances in the second shells, Fig. S9B(2). The outer Ce shells in all samples at >6 Å were formed by Ce/Fe backscattering (to Ce absorber) and were fit with the characteristic Ce-Ce path (of  $\text{Ce}(\text{OH})\text{SO}_4$ ) at 6.53, 6.60, 6.46, and 6.37 Å for Ce, Fe1-Ce2, Ce1-Fe1, and Fe2-Ce1, respectively. Notably, a greater percentage of Fe in the composites slightly reduced the Ce-Ce distance.

### 3.7. FTIR spectra of thermally (300 °C) treated composites, in comparison with composites dried at 80 °C

FTIR spectra of five composites (Fe, Fe2-Ce1, Fe1-Ce1, Fe1-Ce2, and Ce) dried at 80 °C and five samples thermally treated at 300 °C are shown in Figs. S11–S15. A detailed interpretation of IR-active bands in the FTIR spectra of samples dried at 80 °C is given in the companion paper [20]. In that work, it was shown that the spectra of polycrystalline structures of Fe- and Ce-containing composites were highly complex and represented a superposition of different absorption bands of multiphase systems based on Fe and Ce oxide/hydroxides. These systems also included the corresponding carbonates, sulfates, and adsorbed water [32]. As shown previously, the spectra of all samples treated at both temperatures, 80 and 300 °C, showed a broad asymmetric band approximately 3430–3440  $\text{cm}^{-1}$  and a medium-intensity sharp band at 1629  $\text{cm}^{-1}$ , which were due to the bending vibration of water [33]. In addition, in the region above 3600  $\text{cm}^{-1}$  (3736–3743  $\text{cm}^{-1}$ ) low-intensity bands were observed, which correspond to the stretching vibrations of the M-OH hydroxyl groups. Notably, these bands did not disappear due to heat treatment at 300 °C. However, their intensities decreased in FTIR spectra of the thermally treated composites. The major difference in the FTIR spectra of the 80 °C precursors and the composites thermally treated at 300 °C can be seen in the region of carbonate absorption at 1350–1530  $\text{cm}^{-1}$ , which showed a notable reduction or disappearance of the characteristic vibration for carbonate.

Tetrahedral sulfate is usually indicated by a very strong band at approximately 1100  $\text{cm}^{-1}$  (composed mainly by S-O stretch) and another less strong band at approximately 650  $\text{cm}^{-1}$ . The latter is mainly attributed to an umbrella-type motion of the other three sulfate oxygen atoms, resulting from bending vibrations. In a more complicated crystal environment, these bands are usually shifted,

broadened, or split. The shifts due to complexity of the environment can be up to 50  $\text{cm}^{-1}$ . The FTIR spectra of the samples treated at 300 °C show three bands at 1115–1117  $\text{cm}^{-1}$ , 1061–1063  $\text{cm}^{-1}$ , 631, 695 (Fe2-Ce1), and 687 (Fe1-Ce1 and Fe1-Ce2)  $\text{cm}^{-1}$ . These characteristic sulfate features reflect the occurrence of both shifts (of the band at 650  $\text{cm}^{-1}$ ) and splits (of the band at 1100  $\text{cm}^{-1}$ ), compared with tetrahedral sulfate. This might be an additional indication of the localization of sulfate in the interlayer space.

The FTIR spectra of samples treated at 300 °C show broad bands in the region of 400–800  $\text{cm}^{-1}$ . As such, these bands are due to overlapping of the bands from Fe-O and Ce-O vibrations [33]. In comparison with the spectra of two-metal composites treated at 80 °C, this region of the FTIR spectra of samples treated at 300 °C includes multiple bands from stretching M-O vibrations for  $\alpha$ - $\text{Fe}_2\text{O}_3$ ,  $\gamma$ - $\text{Fe}_2\text{O}_3$ , ferrihydrite ( $\text{Fe}_5\text{O}_7(\text{OH})\cdot 4\text{H}_2\text{O}$ ),  $\text{CeO}_2$ , and the new ferric hydroxy-sulfate phase. The last was confirmed by low-intensity absorption bands of stretching Fe-OH vibrations, observed in the region above 3600  $\text{cm}^{-1}$  and by our EXAFS fitting. The IR spectroscopy data are in agreement with the common understanding of the regularities of thermal decomposition in carbonate-containing compounds. Thermal treatment at 300 °C resulted in the decomposition of most carbonate compounds. However, a small amount of carbonate-based substances was left in the structure.

### 3.8. Adsorptive performance of composites treated at 300 °C, in comparison with samples dried at 80 °C

Figs. 6 and 7 compare the adsorptive performances of thermally treated samples with those dried at 80 °C, for five anions, using mg/g and mmol/g as units of adsorption. Three general observations can be made from these figures. Adsorptive removal of arsenate and phosphate was increased in two one-metal composites (Fe and Ce). An exception was the removal of bromate, whose adsorption by the Fe sample was reduced by nearly 20 times. The performances of the “worst” two-metal sample (Fe1-Ce2), obtained at 80 °C, for  $\text{H}_2\text{PO}_4^-$  and  $\text{H}_2\text{AsO}_4^-$  were nearly unchanged after thermal treatment at 300 °C. Finally, in the two best samples obtained at 80 °C (Fe2-Ce1 and Fe1-Ce1) the removal of  $\text{F}^-$  and  $\text{H}_2\text{AsO}_4^-$  was decreased by a factor of nearly two after treatment at 300 °C.

Since the samples treated at 300 °C did not show better performances in the removal of the five selected anions, further adsorption studies (such as those of adsorption isotherms, pH effect, and effect of competing ions) were not conducted. Experimental conditions were chosen to test adsorption at the level of adsorptive capacity. At the initial anion concentration of approximately 200 mg/L, the adsorption isotherms usually yielded a plateau, which indicates saturation of active adsorption sites. An adsorbent dose of 2 g/L also reliably showed an adsorptive performance, as most adsorbents show a plateau in the dependence of adsorptive capacity on the adsorbent dose. The release of Fe and Ce from the material to the adsorbate during adsorption was measured occasionally. The amount of Fe and Ce released into solution was lower than 0.1 and 0.7 mg/L for Fe and Ce, respectively. Although cerium is not considered as very toxic chemical element its concentration shall be measured due to recently recognized possible effect of the long-term exposure and different toxicity of various species, especially, cerium compound nanoparticles [35]. Release of sulfate during adsorption was much lower (<100 mg/L) than the maximum permissible concentration of sulfate in drinking water of 250 mg/L.

Discussion in particular focuses on the correlation between the material structures and their adsorptive performance as resulted from EXAFS, FTIR and XRD studies of ten samples obtained at various experimental conditions.

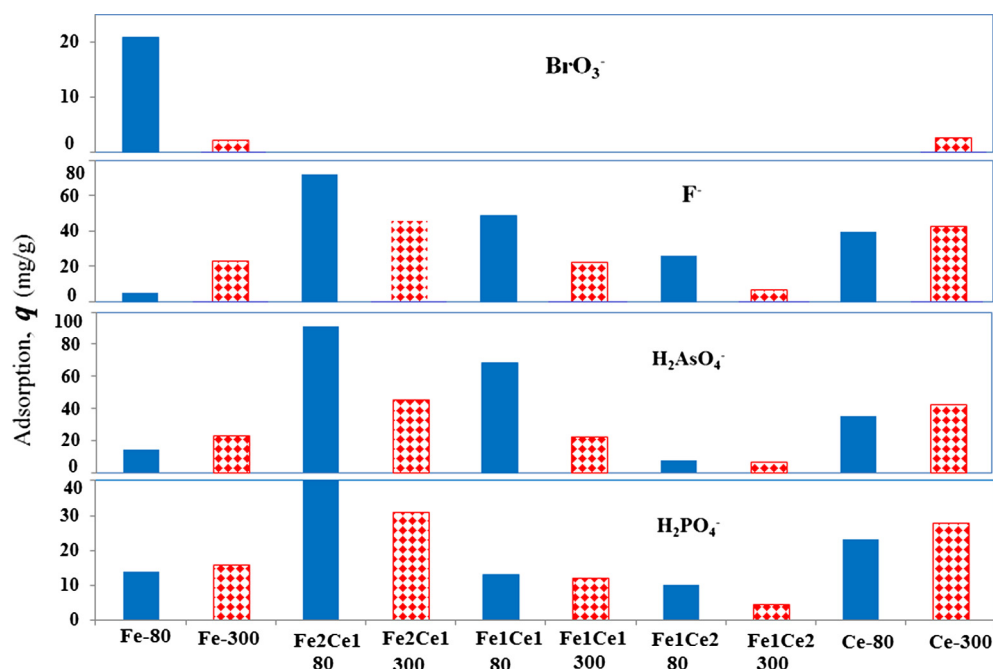


**Fig. 6.** Adsorptive performance of Fe-Ce oxide-based composites treated at 80 and 300 °C in mg/g (A). Experimental conditions: pH =  $6.7 \pm 0.2$ , initial concentration =  $200 \pm 15$  mg/L, adsorbent dose = 2 g/L, ambient temperature ( $20 \pm 2$  °C).

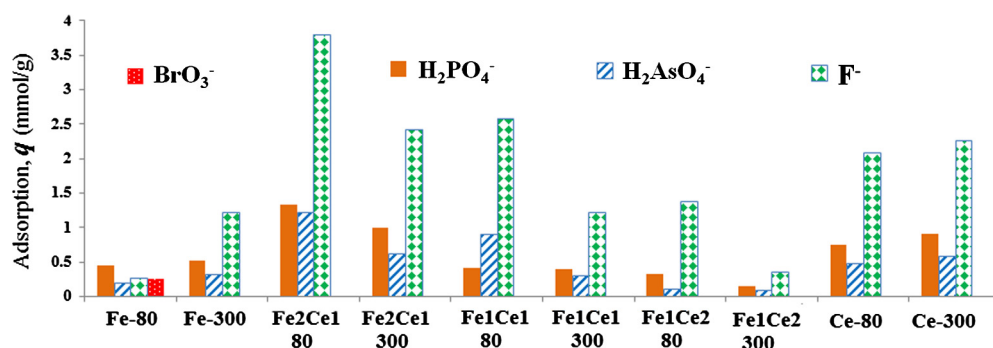


**Fig. 7.** Adsorptive performance of Fe-Ce oxide-based composites treated at 80 and 300 °C in mmol/g.

#### 4. Discussion

Overall, thermal treatments of the inorganic composites based on Fe/Ce hydrous oxides at 300 °C caused root changes in the material mineral composition, compared with samples from the same synthetic batch dried at 80 °C. The local structure around major atoms in the composites obtained at 80 and 300 °C was compared. Additionally, structural changes were associated with adsorptive performance. This allowed the identification of regularities in material structure and its adsorptive removal, which are discussed below.

##### 4.1. Composites based on solo-Fe compounds, Fe

Crystalline phases of the Fe sample obtained at 80 °C, based on Fe hydrous oxides, were composed of maghemite, magnetite, and siderite, as well as the unknown phase with a layered structure. Treatment of this sample at 300 °C resulted in the formation of two new phases, hematite and ferrihydrite, and the elimination of magnetite. As expected, the treatment at 300 °C reduced the  $\text{FeCO}_3$  content from approximately 20% to 10%. However, surprisingly, divalent Fe(II) was left over in the form of siderite species

from the precursor. Interestingly, in spite of the reduced crystallinity of this sample upon thermal treatment, its surface area was unchanged.

The sample treated at 300 °C showed increased removal of arsenate, fluoride, and phosphate, compared with the initial composite dried at 80 °C. However, adsorption of  $\text{BrO}_3^-$  was reduced dramatically. A probable reason for this is the destruction of the new phase, which may have played a leading role in adsorptive removal of bromate. Standard methods of material characterization were not sufficient for establishing regularities between material structure and its removal performance. However, regularities of local structure around Fe and adsorptive removal were established. In particular, it was noted that composites which showed better performances had more backscattering from O atoms (see Fig. 3 and our companion paper [20]). This peculiarity of local structure suggests that increased removal of phosphate, fluoride, and arsenate was associated with two new peaks at  $>4$  Å, fitted with O atoms. We suggest that such features of extended x-ray absorption fine structure most probably indicate active Fe oxide adsorption sites capable of anion exchange with  $\text{OH}^-$ , which further results in the removal of anions by the mechanism of chemisorption. In contrast, adsorption of  $\text{BrO}_3^-$  decreased in the composite treated at 300 °C.

This indicates a different mechanism for the adsorption of bromate onto complex metal oxides, which does not require an abundance of  $\text{OH}^-$  groups but needs some other factor, most probably that of structural correspondence as initiating step.

#### 4.2. Composites based on solo-Ce compounds, Ce

The applied temperature of 300 °C was sufficiently high to cause almost complete transformation of Ce carbonate species into the crystalline phase of ceria ( $\text{CeO}_2$ ) and amorphous cerium hydrous oxides (as shown by XANES). However, a small portion of amorphous Ce carbonate was left in the structure.  $S_{\text{BET}}$  of the 80 °C-sample was increased 7 times (from 11 to 81  $\text{m}^2/\text{g}$ ) after thermal treatment. However, this did not result in a considerable growth of pore volume, nor an increase in the degree of crystallinity. In spite of the dramatic increase in surface area and the formation of new phases whose chemical nature is strictly relevant to the removal of anions (Ce hydrous oxides), the adsorptive performance towards the five anions did not improve considerably. Further, the adsorption of  $\text{F}^-$  onto the composites prepared at 80 and 300 °C was nearly the same. The unchanged adsorptive performance of both (80 and 300 °C) composites was in agreement with the data on the local structure around Ce, obtained by EXAFS simulations. EXAFS modeling demonstrated small differences in the outer shells of the materials treated at 80 and 300 °C. The outer shells of Ce atoms in the samples treated at 300 °C resulted from backscattering of only one O atom, while in the 80 °C-composite, it was formed by two backscattering O atoms. However, no backscattering from heavy atoms Ce/Fe to Ce (absorber) was noted in the outer shells with an extended local environment around Ce in the 80 °C-sample. At the same time, the content of surface sulfate (from XPS) was nearly the same in the composites treated at both 80 and 300 °C. This observation most probably indicates that surface sulfate was a major functional group responsible for anion exchange in both composites. This is most probably because sulfate was an energetically favorable site for adsorption, compared to the other anion exchange sites, such as  $\text{OH}^-$ .

#### 4.3. Two-metal composites from Fe-Ce-oxide based compounds: Fe2-Ce1, Fe1-Ce1, Fe1-Ce2

When the two-metal precursors dried at  $20 \pm 2$  °C were thermally treated at 300 °C, considerable changes were observed in their compositions. Such considerable transformations were facilitated by the presence of Ce carbonate species in the precursor structure. In particular, a considerable increase in surface area (2–3 times) and pore volume (of two of them) was observed. Additionally, there was a dramatic increase in the degree of crystallinity, compared with the composites prepared at 80 °C. The increase in crystallinity was largely due to the formation of the novel (unknown) Fe-based layered compounds with the interlayer sulfate and possibly, carbonate. The Fe-components of the three two-metal samples were composed of two crystalline phases (one of which was the new phase, hematite) and amorphous hydrous iron oxides. There were differences in the ratios of various Fe compounds in the three materials (XANES LCF). The Ce-component in all bimetal samples was composed of one crystalline phase,  $\text{CeO}_2$ , and of amorphous Ce hydrous oxides. In addition, there was a small portion of Ce carbonates (2.1–6.6%) in the structure, compared with 93–100% of Ce carbonate species in the composites dried at 80 °C.

Overall, improved adsorptive removal was expected upon thermal treatment at 300 °C. More phases of the relevant chemical nature and a much higher surface area are expected to increase the general surface reactivity of the material. In addition, the newly formed layered hydrous oxides can theoretically act by the mech-

anism of second-anion exchange and are able to host anions within their interlayer space. On the contrary, the overall adsorptive performance of composites treated at 300 °C was reduced in comparison to the samples treated at 80 °C.

In summary, EXAFS modeling showed the difference in local structures of outer shells of composites treated at 80 and 300 °C, produced from the same synthetic batch. The extended x-ray absorption fine structures around Fe in the two best 80 °C-samples, Fe2-Ce1 and Fe1-Ce1, were rich in backscattering from both Fe and O to the Fe absorber. However, these extended structures disappeared after thermal treatment at 300 °C. This was correlated with the decrease in adsorptive removal of  $\text{F}^-$ ,  $\text{H}_2\text{PO}_4^-$ , and  $\text{H}_2\text{AsO}_4^-$ , which most probably indicates a loss of active adsorptive sites. Interestingly, the adsorption performances of the sample Fe1-Ce2 to  $\text{H}_2\text{PO}_4^-$  and  $\text{H}_2\text{AsO}_4^-$  were nearly the same after treatment at 80 and 300 °C. This is also consistent with the nearly unchanged local structure around Fe in the outer shells in these two materials. On the other hand, surface sulfate, which played an important role in adsorption by the composites prepared at 80 °C, was transformed into a layered compound upon treatment at 300 °C. Therefore, it probably was not involved in the removal. This might be another reason for the reduced removal performance of the two-metal composites treated at 300 °C. However, EXAFS simulations reflect the local structure of the entire material, including the aforementioned phase.

#### 4.4. Hypothesis for utilization of extended structure from EXAFS in estimation of surface reactivity during adsorption and catalysis

To the best of our knowledge, EXAFS simulations of local structures around atoms have not yet been used to correlate the atomic structure of a material with its adsorptive removal performance in water. Therefore, a comparison with the literature is impossible. This work confirms our hypothesis, first expressed in the companion paper [20], that the adsorptive performance of inorganic anion exchangers based on metal hydrous oxides can be predicted from the local structures around the metals comprising the adsorbent. Here, these local structures were simulated by EXAFS. We think that in order for an oxide-based material to be a strong anion remover, an extended structure must form around the metal, as a result of backscattering from both the metal and oxygen. The formation of such an extended structure is reflected by, for example, {Fe-Fe}+{Fe-O} distances in outer shells. This hypothesis is based on the comparison of outer shells of Fe and Ce and the degree of anion removal by the material, as shown above. It is suggested that such characteristic features of the extended local structure correlate with the content and/or availability of  $\text{OH}^-$  adsorption sites.

#### 4.5. Bimetal composites from Fe-Ce-oxide-based compounds: hybrid or mixed materials?

Simulations of Fe and Ce EXAFS data, supported by XRD patterns and FTIR spectra, were used to draw conclusions about hybridization in Fe-Ce oxide-based systems treated thermally at 300 °C. Fe K-edge EXAFS spectra and XRD patterns demonstrated the formation of novel phases based on layered two-metal oxides. We assume that the new layered compounds are mainly composed of Fe(II)/Fe(III) layered hydroxides in which Ce substitutes some atoms of Fe in the structure. This provides suggestion for the formation of one type of hybrid systems upon thermal treatment.

The formation of solid solutions can also be concluded from a comparison of XRD patterns of samples dried at 80 °C and composites thermally treated at 300 °C. In particular, an unknown novel phase with a layered structure was formed in the Fe sample dried at 80 °C. However, this new phase disappeared upon treatment at 300 °C. On the other hand, the presence of two metals in the

composites dried at 80 °C resulted in the formation of a similar new layered structure. These observations demonstrate that the novel layered structures in two-metal 300 °C-composites were formed due to the presence of both metals, which were a necessary structural part of the novel layered phases.

Ce L<sub>3</sub>-edge EXAFS spectra also suggested the formation of solid solutions. This was concluded from the 1st shell of the local structure around Ce. The broader shapes of the 1st shells of the Ce-component (Ce-O) in the two-metal samples (which was most distinct for the Fe-dominant composition, Fe<sub>2</sub>-Ce<sub>1</sub>) indicated the formation of solid solutions. On the other hand, there might have been an overlap of the two backscattering oscillations from two O atoms to the Ce absorber. When the Fe-content in the dosage was twice as high, the portion of solid solution was increased. This resulted in considerable broadening of the 1st shell of Ce. Analysis of the 1st shell around Mn atoms was also conducted by Lee and co-authors [34], to characterize the solid solutions of MnCO<sub>3</sub>-CaCO<sub>3</sub>. This analysis was based on the comparison of 1st-shell Mn-O and Ca-O distances in the theoretical structures of carbonates and in the experimental samples. In conclusion, the combination of EXAFS and XRD data confirmed the formation of solid solutions in the two-metal composites (xFe-yCe) upon thermal treatment at 300 °C.

It has been proven by numerous studies that hybridization between inorganic phases improves many applications associated with high surface reactivity. However, similar observations were not obtained in this work, which associated the surface reactivity reflected in x-ray absorption fine structure with adsorptive removal from water. Hybrid phases were formed upon treatment at 300 °C. However, no notable increase was observed in the adsorption of five anions. We think that the presence of the newly formed hybrid phases might improve the catalytic performances of many processes. It is very possible that these materials will show different performances in air purification or catalysis.

## 5. Conclusions

The urea-based hydrothermal precipitation approach has proven to be an excellent synthetic method for the fabrication of both mono- and two-metal hydrous oxides, with flexibility of phase transformation upon thermal treatment. Using this approach, ten new composites were synthesized. These were based on hydrous oxides of Fe and Ce at five dosage ratios (1:0, 2:1, 1:1, 1:2, and 0:1), denoted here as Fe, Fe<sub>2</sub>-Ce<sub>1</sub>, Fe<sub>1</sub>-Ce<sub>1</sub>, Fe<sub>1</sub>-Ce<sub>2</sub>, and Ce, respectively. Five of these ten composites were obtained by thermal treatment at 300 °C, while the other five materials from the same synthetic batch were dried at 80 °C. A reasonably low temperature of 120 °C during synthesis resulted in the formation of a Ce-carbonate-based Ce component, which was transformed into ceria at 300 °C. The presence of Ce carbonate species in two-metal composites promoted dramatic changes in the composite compositions, resulting in the formation of novel phases consisting of Fe/Ce layered hydrous oxides with interlayer sulfate and possibly, carbonate.

The removal performances of five anions (arsenate, phosphate, fluoride, bromate, and bromide) by the ten materials did not correlate with their porous properties (such as surface area). However, the removal performances were well-correlated with the local structures around Ce, and especially around Fe atoms. It has been proven that heterogeneity, surface functionality, and availability of adsorption sites, which usually facilitate the chemisorption mechanism, are the main properties to be designed in inorganic anion exchangers based on metal hydrous oxides. The quality of such a material can be estimated from the local structures around the metal atoms which compose the oxide-based material, as sim-

ulated by EXAFS. This is the first methodological approach suggested for the estimation of adsorptive and possibly, catalytic properties of inorganic ion exchangers. The estimation is based on the extended x-ray absorption fine structure around major atoms of metal oxides, with particular focus on outer shells. The suggested approach resulted from the interpretation of data presented in two companion papers. These data were based on Fe/Ce EXAFS simulations, XANES analysis, porous properties, XRD patterns, FTIR spectra, and association of the above with the anion removal performance.

Overall, two-metal composites formed at Fe ≥ Ce dosage ratios and dried at 80 °C showed the best anion adsorption, including exceptional removal of toxic arsenate and excess fluoride, and this correlated with the rich structure of outer shells of Fe. Notably, composites dried at 80 °C had not yet formed hybrid materials. The adsorptive capacity of 80 °C-Fe<sub>2</sub>-Ce<sub>1</sub> for F<sup>-</sup>, obtained from equilibrium isotherms at pH = 7, was exceptionally high and reached 160 mg[F]/g. Outer shells of Fe in the composite Fe<sub>2</sub>-Ce<sub>1</sub> were rich in structure, which resulted from backscattering from both Fe and O atoms. In our opinion, the strong outer shells formed by both Fe and O reflect the presence of active anion-exchange sites, OH<sup>-</sup>, on Fe-component. In contrast, the loss of extended x-ray absorption fine structure, particularly the features resulting from backscattering from O atoms, upon treatment at 300 °C is correlated with a decrease in adsorptive removal.

Future studies will investigate the phase transformations in these materials upon treatment at temperatures higher than 300 °C. Their catalytic activities in the relevant processes and their removal performance from air will also be studied. Another interesting scientific question to address is whether (and how) the chemical composition (two metals versus one metal composites) influences the richness of the extended x-ray absorption fine structures. Most probably more research tools shall be used.

## Acknowledgments

This work was funded by King Abdullah University of Science and Technology (KAUST) via the Global Research Partnership Programme, award N° KUK-C1-017-12, and Netherlands Organization for Scientific Research (NWO) for EXAFS/XANES studies at the Dutch-Belgian Beamline (DUBBLE) at the European Synchrotron Radiation Facilities (ESRF). The authors are grateful to Dr. Andrey Shchukarev (Umea University) for XPS measurements and consideration of the results and to Ms. Helen de Waard, Ms. Dineke van de Meent-Olieman, Ms. Anita van Leeuwen-Tolboom, Mr. Pieter Kleingeld, Mr. Piet Peereboom, and Mr. Ton Zalm (Utrecht University) for excellent technical support during their research. The authors gratefully acknowledge the anonymous Reviewers and Editor Prof. Teresa Bandoz for helping improve this work.

## Appendix A. Supplementary material

Supplementary data associated with this article can be found, in the online version, at <http://dx.doi.org/10.1016/j.jcis.2016.12.008>.

## References

- [1] J. Zhu, Z. Zhu, H. Zhang, H. Lu, Y. Qiu, L. Zhu, S. Küppers, *J. Colloid Interface Sci.* 481 (2016) 144–157.
- [2] L. Zhu, Z. Zhong, H. Yang, C. Wang, *J. Colloid Interface Sci.* 478 (2016) 11–21.
- [3] M. Cao, P. Wang, Y. Ao, C. Wang, J. Hou, J. Qian, *J. Colloid Interface Sci.* 467 (2016) 129–139.
- [4] A. Umar, R. Kumar, M.S. Akhtar, G. Kumar, S.H. Kim, *J. Colloid Interface Sci.* 454 (2015) 61–68.
- [5] B. Bhaduri, N. Verma, *J. Colloid Interface Sci.* 436 (2014) 218–226.
- [6] Z. Lu, C. Mao, M. Meng, S. Liu, Y. Tian, L. Yu, B. Sun, C. Ming Li, *J. Colloid Interface Sci.* 435 (2014) 8–14.

- [7] K. Gupta, S. Bhattacharya, D. Nandi, A. Dhar, A. Maity, A. Mukhopadhyay, D.J. Chattopadhyay, N.R. Ray, P. Sen, U.C. Ghosh, J. Colloid Interface Sci. 377 (2012) 269–276.
- [8] S. Rajput, C.U. Pittman Jr., D. Mohan, J. Colloid Interface Sci. 468 (2016) 334–346.
- [9] S.N. Shah, A.A. Khan, A. Espinosa, M.A. Garcia, W. Nuansing, M. Ungureanu, J.G. Hedde, A.L. Chuvilin, C. Wege, A.M. Bittner, Langmuir 32 (2016) 5899–5908.
- [10] A. Trovarelli, Catalysis by Ceria and Related Systems, Imperial College Press, London, 2002.
- [11] Y. Nagai, T. Yamamoto, T. Tanaka, T. Nonaka, A. Suda, Phys. Scr. (2005) T115 (conference proceeding).
- [12] Y. Nagai, T. Yamamoto, T. Tanaka, S. Yoshida, T. Nonaka, T. Okamoto, A. Suda, M. Sugiura, J. Synchrotron Radiat. 8 (2001) 616–618.
- [13] F.J. Perez-Alonso, I. Melián-Cabrera, M. López Granados, F. Kapteijn, J.L.G. Fierro, J. Catal. 239 (2006) 340–346.
- [14] F.J. Perez-Alonso, M. Lopez Granados, M. Ojeda, P. Terreros, S. Rojas, T. Herranz, J.L.G. Fierro, Chem. Mat. 17 (2005) 2329–2339.
- [15] Q. Yang, Z. Lu, J. Liu, X. Lei, Z. Chang, L. Luo, X. Sun, Prog. Nat. Sci.: Mater. Int. 23 (2013) 351–366.
- [16] A. Kajiyama, Nakamura, Colloids Surfaces: A 163 (2000) 301–307.
- [17] R. Si, Y.W. Zhang, S.J. Li, B.X. Lin, C.H. Yan, J. Phys. Chem. B 108 (2004) 12481–12488.
- [18] S. Music, M. Maljkovic, I. Czako-Nagy, Mater. Lett. 31 (1997) 43–48.
- [19] S. Music, S. Popovic, M. Gotic, J. Mater. Sci. 25 (1990) 3186–3190.
- [20] N. Chubar, V. Gerda, D. Banerjee, G. Yablokova, J. Colloid Interface Sci. 487 (2017) 388–400.
- [21] S. Nikitenko, A. Beale, A. van der Eerden, S. Jacques, U. Leynaud, M. O'Brien, D. Detollenaere, F. Kaptein, R.B. Weckhuysen, W. Bras, J. Synchr. Radiat. 15 (2008) 632.
- [22] B. Ravel, M. Newville, J. Synchr. Radiat. 12 (2005) 537.
- [23] data base at <<http://cars9.uchicago.edu/cgi-bin/atoms>>.
- [24] C. Wan, S. Ghose, G.R. Rossman, Am. Miner. 63 (1978) 478–483.
- [25] L. Fanfani, A. Nunzi, P.F. Zanazzi, Am. Miner. 56 (1971) 751–757.
- [26] [http://materials.springer.com/isp/crystallographic/docs/sd\\_0308561](http://materials.springer.com/isp/crystallographic/docs/sd_0308561).
- [27] S. Yin, Y. Minamidate, S. Tonouchi, T. Goto, Q. Dong, H. Yamate, T. Sato, RSC Adv. 2 (2012) 5976–5982.
- [28] L.-W. Qian, X. Wang, H.-G. Zheng, Cryst. Growth Des. 12 (2012) 271–280.
- [29] Y. Yang, L.-H. Zhu, M.-H. Zeng, X.-L. Feng, Acta Cryst. E61 (2005) i41–i43.
- [30] C. Cismasu, K.H. Williams, P.S. Nico, Environ. Sci. Technol. 50 (2016) 25–35.
- [31] L.-W. Qian, X. Wang, H.-G. Zheng, Crystal Growth Des. 12 (2012) 271–280.
- [32] F.A. Miller, C.H. Wilkins, Anal. Chem. 24 (1952) 1253–1294.
- [33] K. Nakamoto, Infrared and Raman Spectra of Inorganic and Coordination Compounds. Part A. Theory and Applications in Inorganic Chemistry, fifth ed., John Wiley & Sons Inc., New York, 1997.
- [34] Y.J. Lee, R.J. Reeder, R.W. Wenskus, E.J. Elzinga, Phys. Chem. Miner. 29 (2002) 585–594.
- [35] J.T. Dahle, Y. Araj, Int J. Environ. Res. Public Health 12 (2015) 1253–1278.